J. Fluid Mech. (2018), *vol.* 836, *pp.* 304–323.
doi:10.1017/jfm.2017.816

Bistability in the synchronization of actuated microfilaments

Hanliang Guo[1], Lisa Fauci[2], Michael Shelley[3,4] and Eva Kanso[1,3,†]

[1]Aerospace and Mechanical Engineering, University of Southern California, Los Angeles, CA 90089, USA

[2]Department of Mathematics, Tulane University, New Orleans, LA 70118, USA

[3]Center for Computational Biology, Flatiron Institute, Simons Foundation, New York, NY 10010, USA

[4]Courant Institute of Mathematical Sciences, New York University, New York, NY 10012, USA

(Received 4 August 2017; revised 8 October 2017; accepted 6 November 2017)

Cilia and flagella are essential building blocks for biological fluid transport and locomotion at the micrometre scale. They often beat in synchrony and may transition between different synchronization modes in the same cell type. Here, we investigate the behaviour of elastic microfilaments, protruding from a surface and driven at their base by a configuration-dependent torque. We consider full hydrodynamic interactions among and within filaments and no slip at the surface. Isolated filaments exhibit periodic deformations, with increasing waviness and frequency as the magnitude of the driving torque increases. Two nearby but independently driven filaments synchronize their beating in-phase or anti-phase. This synchrony arises autonomously via the interplay between hydrodynamic coupling and filament elasticity. Importantly, in-phase and anti-phase synchronization modes are bistable and coexist for a range of driving torques and separation distances. These findings are consistent with experimental observations of in-phase and anti-phase synchronization in pairs of cilia and flagella and could have important implications on understanding the biophysical mechanisms underlying transitions between multiple synchronization modes.

Key words: biological fluid dynamics, low-Reynolds-number flows, nonlinear dynamical systems

1. Introduction

Cilia and flagella exhibit synchronous motion. The biflagella of the alga *Chlamydomonas* often beat symmetrically at the same frequency but opposite phase (Rüffer & Nultsch 1985, 1987; Goldstein, Polin & Tuval 2009, 2011; Polin *et al.* 2009). Sperm cells tend to synchronize their tail beating in-phase when they are in close proximity (Gray 1928; Woolley *et al.* 2009). Motile cilia in aquatic organisms and in mammalian tissues coordinate their collective beating in a wavelike pattern (Brennen & Winet 1977; Fulford & Blake 1986; Brumley *et al.* 2012).

The origin of this synchronous behaviour is attributed to mechanical coupling between the cilia, either at the cell base (Quaranta, Aubin-Tam & Tam 2015; Wan

† Email address for correspondence: kanso@usc.edu

& Goldstein 2016) or through hydrodynamics (Brumley *et al.* 2014). In the latter, the flagella of isolated cells exhibit synchronous beating through hydrodynamics only. Theoretical models also suggest that synchronization can arise from hydrodynamic coupling between flagella (Guirao & Joanny 2007; Golestanian, Yeomans & Uchida 2011; Mettot & Lauga 2011; Uchida & Golestanian 2011, 2012), assisted by flagellar elasticity (Elfring & Lauga 2011; Goldstein *et al.* 2016). Existing models are based either on low-order representations of flagella and cilia in the form of 'bead–spring' oscillators (Niedermayer, Eckhardt & Lenz 2008; Kotar *et al.* 2010; Golestanian *et al.* 2011; Bruot *et al.* 2012) or on more realistic models of hydrodynamically coupled elastic filaments (Kim & Netz 2006; Osterman & Vilfan 2011; Goldstein *et al.* 2016). These models primarily reproduce one mode of synchrony: anti-phase, in-phase or metachronal coordination. Flagellar synchrony is more complex: flagella and cilia can exhibit multiple synchronization modes even within a single cell type or organism. For example, the flagella of the algae *Chlamydomonas* stochastically switch between anti-phase and in-phase synchrony (Leptos *et al.* 2013; Wan, Leptos & Goldstein 2014). Cilia in mammalian brain ventricles periodically change their collective beat orientation, providing a cilia-based switch for redirecting the transport of cerebrospinal fluid at regular intervals of time (Faubel *et al.* 2016). The origins of these transitions, whether abrupt and stochastic (*Chlamydomonas* biflagellates) or gradual and periodic (ependymal cilia), are currently unknown.

In models that represent flagella as hydrodynamically coupled oscillators driven by a configuration-dependent force, the functional dependence of this force on configuration needs to be altered in order for the system to exhibit a different mode of synchrony – see Bruot & Cicuta (2016) for review. The need to modify the functional form of the drive, and consequently the landscape of the associated potential field, makes implicit assumptions on the mechanisms responsible for different modes of synchrony. It assumes that these mechanisms induce a fundamental change in the internal machinery that drives the flagellum or cilium beyond what can be captured by rescaling the intensity of the drive. In this study, we present a theoretical model of flow-coupled elastic filaments that exhibits bistable in-phase and anti-phase synchronization at the same drive level, suggesting that the aforementioned assumption is not required to achieve multiple synchronization modes.

The synchronization of filaments in a viscous fluid has been studied since the seminal work of Taylor (1951), where he showed that travelling waves in two parallel infinite sheets have the least viscous dissipation when synchronized in-phase. These results were later extended to include waveform compliance (Elfring & Lauga 2011) and three-dimensional (3D) beating (Mettot & Lauga 2011). Olson & Fauci (2015) considered elastic sheets and filaments of finite length and computationally showed that neighbouring sheets and filaments with symmetric beating patterns always synchronize in-phase. In-phase synchrony was also predicted by Goldstein *et al.* (2016). A model of cilia that accounted for internal actuation also demonstrated that neighbouring cilia, coupled only through hydrodynamics, quickly synchronize their beat (Yang, Dillon & Fauci 2008).

Cilia and flagella are driven into oscillatory motion by an intricate internal structure of microtubules and molecular motors. Although the components of this structure are known, the mechanisms that regulate the activity of the internal motors, causing them to produce oscillatory motions are not well understood. A prominent hypothesis assumes a geometric feedback from mechanical deformations to molecular activity (Brokaw 1971, 2009; Riedel-Kruse *et al.* 2007; Sartori *et al.* 2016). In its simplest form, this hypothesis supports the view that the internal forces and moments produced

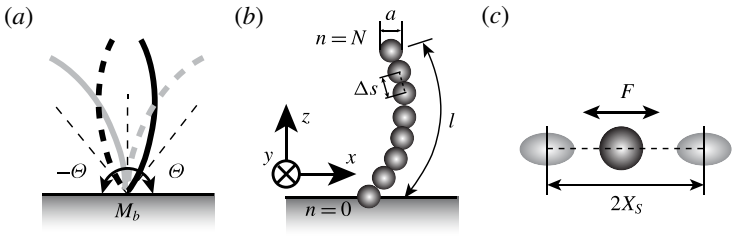

FIGURE 1. (*a*) Elastic filament actuated by a motor at its base with configuration-dependent bending moment $\boldsymbol{M}_b$. The moment switches direction when the tangent to the base reaches predefined target angles $\pm\Theta$. (*b*) Discretization of the elastic filament into $N+1$ spheres of diameter a. (*c*) Low-order model of a shape-dependent oscillator driven by an applied force F that switches directions once the oscillator reaches a predefined oscillation amplitude $|x| = X_s$.

by the molecular motors switch 'on' and 'off' depending on the shape of the flagellum.

Inspired by this switching behaviour, Kotar *et al.* (2010) and Bruot *et al.* (2012) proposed optically driven colloidal oscillators as a model system for studying synchronization between cilia and flagella. In these systems, the colloidal particle is constrained to move on a linear trajectory under the influence of a driving force that switches direction once the particle approaches predefined target positions, hence the name 'geometric switch'. Here, we extend the geometric switch model to finite microfilaments submerged in viscous fluid and driven at their base by an active bending moment, of constant magnitude, that switches direction at predefined orientations of the tangent at the filament's base. This model of internal actuation is a simplification of the biological system where actuation is applied along the filament's centreline. Yet, it carries some common features such as feedback from filament shape to internal drive. It is also reminiscent to the model used in Kim & Netz (2006) (although conceived independently), who applied a non-constant drive moment to induce asymmetry in the filament's beat pattern for studying metachronal wave coordination of neighbouring filaments. Our study focuses on the existence of multiple modes of synchronization at constant drive magnitude. We find that single filaments exhibit time-periodic deformations that seem to be insensitive to the initial configuration of the filament, and we quantify the consequent frequency of these deformations. We then show that two hydrodynamically coupled filaments can achieve in-phase and anti-phase synchronizations that are bistable for a range of parameter values. To highlight the main physical mechanisms responsible for these synchronization modes, we introduce a low-order particle model that accounts for elasticity and shape changes. The simpler model indicates that bistable synchronizations emerge as a result of hydrodynamic coupling, shape changes and an internal restoring moment due to filament elasticity. We conclude by commenting on the relevance of these results to understanding the biophysical mechanisms underlying transitions between multiple synchronization modes in flagella and cilia.

2. Continuum model

Consider a nearly inextensible elastic filament of length ℓ and diameter a rooted at the origin O of a Cartesian coordinate system (x, y, z). Let $\{\boldsymbol{e}_1, \boldsymbol{e}_2, \boldsymbol{e}_3\}$ be the

corresponding orthonormal basis. The filament is free to deform in the half-space fluid domain $z \geqslant 0$, where $z = 0$ corresponds to a no-slip solid wall (see figure 1). The centreline of the filament is denoted by the position vector $\boldsymbol{r}(s, t)$, where s and t represent the arclength and time, respectively. The balance of forces and moments on a cross-section of the filament are given by Kirchhoff's equations for an elastic rod (Audoly & Pomeau 2010)

$$\boldsymbol{N}' - \boldsymbol{f} = \boldsymbol{0}, \quad \boldsymbol{M}' + \hat{\boldsymbol{t}} \times \boldsymbol{N} = \boldsymbol{0}. \tag{2.1a,b}$$

Here, the prime $(\cdot)' = \partial(\cdot)/\partial s$ denotes differentiation with respect to arclength s, $\hat{\boldsymbol{t}} = \boldsymbol{r}'/|\boldsymbol{r}'|$ is the tangent unit vector along the filament centreline, $\boldsymbol{N}$ and $\boldsymbol{M}$ are the internal force and bending moment, respectively, and $-\boldsymbol{f}$ is the drag force per unit length exerted by the surrounding fluid on the filament ($\boldsymbol{f}$ is the force per unit length exerted by the filament on the fluid). The Hookean constitutive relation between the bending moment $\boldsymbol{M}$ and the bending deformation (curvature) of the filament is given by $\boldsymbol{M} = B\hat{\boldsymbol{t}} \times \hat{\boldsymbol{t}}'$, where B is the bending rigidity. The internal force $\boldsymbol{N}$ consists of a bending force and a constraint tension force that enforces the inextensibility condition. The constraint is satisfied in a weak form by considering an elastic filament with large tensile stiffness.

The filament is free at its tip $s = \ell$ and is actuated by an internal motor at its base $s = 0$ that produces a torque $\boldsymbol{M}(0, t) = \boldsymbol{M}_b$. The torque $\boldsymbol{M}_b$ is a configuration-dependent torque that switches direction when the base angle $\theta_b(t)$ of the filament, defined as $\theta_b = \arcsin(\boldsymbol{e}_3 \times \hat{\boldsymbol{t}}(0, t) \cdot \boldsymbol{e}_2)$, reaches predefined target orientations $\pm\Theta$. More specifically, we consider $\boldsymbol{M}_b = \alpha M_b \boldsymbol{e}_2$, where M_b is a positive constant and $\alpha \in \{-1, 1\}$ is a state variable that defines the torque direction; α changes from 1 to -1 at $\theta_b = \Theta$ and from -1 to 1 at $\theta_b = -\Theta$ (see figure 1). This torque model can be viewed as an extension to the geometric switch model for colloidal systems studied in Kotar *et al.* (2010) and Bruot *et al.* (2012), and as a simplified version of the 'geometric clutch' model proposed in Lindemann (1994). A target angle that acts as a geometric switch to drive elastic filaments along their entire length was used by Buchmann, Cortez & Fauci (2017) to model the power and recovery strokes of eukaryotic cilia.

The fluid motion is governed by the incompressible Stokes equation for zero-Reynolds-number flows,

$$-\boldsymbol{\nabla} p + \mu \nabla^2 \boldsymbol{u} + \boldsymbol{F} = 0, \quad \boldsymbol{\nabla} \cdot \boldsymbol{u} = 0. \tag{2.2a,b}$$

Here, p is the pressure field, μ is the fluid viscosity, $\boldsymbol{u}$ is the fluid velocity field, and $\boldsymbol{F}$ is the (Eulerian) force density exerted by the filament on the fluid. The last, $\boldsymbol{F}(\boldsymbol{x}, t)$, is related to the force per unit length $\boldsymbol{f}(s, t)$ as $\boldsymbol{F}(\boldsymbol{x}, t) = \int_{s\in[0,\ell]} \boldsymbol{f}(s, t)\delta(\boldsymbol{x} - \boldsymbol{r}(s, t))\,\mathrm{d}s$, where δ is the 3D Dirac δ-function and $\boldsymbol{x}$ is the position vector. These equations are subject to the no-slip condition $\boldsymbol{u} = 0$ at the bounding wall $z = 0$. We take advantage of the small aspect ratio $a/\ell \ll 1$ of the filament to approximate the velocity at the filament boundary by the velocity along its centreline,

$$\boldsymbol{u}|_{filament} = \dot{\boldsymbol{r}}(s, t). \tag{2.3}$$

To fully determine the filament deformation $\boldsymbol{r}(s, t)$ given the moment $\boldsymbol{M}_b$ at the filament base, we need to solve the coupled fluid–filament system of equations (2.1)–(2.3). It is convenient for building an efficient numerical method to (i) write the moment equation in (2.1) in integral form and (ii) assume that the filament is quasi-inextensible (Teran, Fauci & Shelley 2010; Chrispell, Fauci & Shelley 2013;

Parameter	Symbol	Dimensional value
Filament length	ℓ	20 μm
Fluid viscosity	μ	10^{-3} Pa s
Bending rigidity	B	800 pN μm^2
Time scale	$T=\dfrac{\ell^4\mu}{B}$	0.2 s

TABLE 1. Characteristic scales of the system.

Olson & Fauci 2015). In particular, we integrate the moment equation in (2.1) from the filament free end at ℓ to any location s along the filament, taking into account that $\boldsymbol{M}(\ell)=0$ and that along the filament $\boldsymbol{N}'=\boldsymbol{f}$. We get, after an integration by parts on the second term, that

$$\boldsymbol{M}(s)+\boldsymbol{r}\times\int_{\ell}^{s}\boldsymbol{f}\,\mathrm{d}\tilde{s}-\int_{\ell}^{s}\boldsymbol{r}\times\boldsymbol{f}\,\mathrm{d}\tilde{s}=\boldsymbol{0}. \tag{2.4}$$

We then write the force density $\boldsymbol{f}(s,t)$ applied by the filament on the surrounding fluid as $\boldsymbol{f}=\boldsymbol{f}^{\perp}+\boldsymbol{f}^{\parallel}$. We assume that the force component $\boldsymbol{f}^{\parallel}=(\boldsymbol{f}\cdot\hat{\boldsymbol{t}})\hat{\boldsymbol{t}}$ tangent to the filament's centreline can be obtained explicitly by considering a large tensile stiffness K,

$$\boldsymbol{f}^{\parallel}=-K|\boldsymbol{r}'|'\hat{\boldsymbol{t}}, \tag{2.5}$$

thus ensuring that the filament's length remains almost constant. We substitute (2.5) into (2.4) taking into account that $\boldsymbol{M}=B\boldsymbol{r}'\times\boldsymbol{r}''$ to obtain an expression for $\boldsymbol{f}^{\perp}$ in terms of the position vector $\boldsymbol{r}(s)$ and its spatial derivatives. To this end, one gets both components of the force density $\boldsymbol{f}=\boldsymbol{f}^{\perp}+\boldsymbol{f}^{\parallel}$ in terms of the kinematic variables $\boldsymbol{r}$ and its derivatives. We substitute these expressions for $\boldsymbol{f}$ into (2.2) and we solve numerically subject to (2.3) to obtain the nonlinear dynamics of the filament, as discussed next.

To obtain non-dimensional counterparts to the equations of motion, we consider the dimensional scales associated with the fluid viscosity μ and cilium length ℓ. Because of the geometric switch model, the system does not have an intrinsic time scale. To remedy this, we consider the time scale $T=\ell^4\mu/B$ arising from balancing the filament's elasticity with the fluid viscosity. To this end, we consider the bending rigidity to be of the order $B=800$ pN μm^2, as reported in Xu *et al.* (2016) for wild-type *Chlamydomonas* flagella. A list of the dimensional parameters used to scale the equations of the motion is reported in table 1. Hereafter, all quantities are considered to be dimensionless unless otherwise stated.

3. Numerical method

We discretize the filament into a uniform chain of $N+1$ segments of length a such that $\Delta s=\ell/N=a$ (figure 1*b*). The segments are labelled from $n=0$ at the filament base to $n=N$ at its tip. The position vector is discretized by $\boldsymbol{r}_n=x_n\boldsymbol{e}_1+z_n\boldsymbol{e}_3$ and the local orientation θ_n of the tangent vector to segment n is defined as the angle between the z-axis and the vector $\Delta\boldsymbol{r}_n=(\boldsymbol{r}_{n+1}-\boldsymbol{r}_n)$. Equation (2.4) can be written in discrete form as

$$\boldsymbol{M}_{n-1}-\sum_{m\geqslant n}^{N}[(\boldsymbol{r}_m-\boldsymbol{r}_{n-1})\times\boldsymbol{f}_m]=\boldsymbol{0}. \tag{3.1}$$

Here, $\boldsymbol{M}_n = -B[(\theta_n - \theta_{n-1})/\Delta s]\boldsymbol{e}_2$ for $1 \leqslant n < N$ whereas $\boldsymbol{M}_o = \boldsymbol{M}_b$ at the no-slip wall $z = 0$.

We decompose the force $\boldsymbol{f}_n = \boldsymbol{f}_n^{\perp} + \boldsymbol{f}_n^{\parallel}$ exerted by segment n on the surrounding fluid into two components, $\boldsymbol{f}_n^{\perp}$ and $\boldsymbol{f}_n^{\parallel}$, that are perpendicular and parallel to $\Delta\boldsymbol{r}_{n-1} = (\boldsymbol{r}_n - \boldsymbol{r}_{n-1})$. We substitute into (3.1) and rearrange the term containing $\boldsymbol{f}_n^{\perp}$ to the other side of the equation to get

$$\Delta\boldsymbol{r}_{n-1} \times \boldsymbol{f}_n^{\perp} = \boldsymbol{M}_{n-1} - \sum_{m>n}^{N} [(\boldsymbol{r}_m - \boldsymbol{r}_{n-1}) \times \boldsymbol{f}_m]. \tag{3.2}$$

Upon taking the cross-product with $\Delta\boldsymbol{r}_{n-1}/\|\Delta\boldsymbol{r}_{n-1}\|^2$, the above equation becomes

$$\boldsymbol{f}_n^{\perp} = \left[\boldsymbol{M}_{n-1} - \sum_{m>n}^{N} (\boldsymbol{r}_m - \boldsymbol{r}_{n-1}) \times \boldsymbol{f}_m\right] \times \frac{\Delta\boldsymbol{r}_{n-1}}{\|\Delta\boldsymbol{r}_{n-1}\|^2}. \tag{3.3}$$

The parallel component $\boldsymbol{f}_n^{\parallel}$ is given by the discrete analogue to (2.5). Namely, for $1 \leqslant n < N$, one has

$$\boldsymbol{f}_n^{\parallel} = -K\left[-\frac{\|\Delta\boldsymbol{r}_n\| - \Delta s}{\Delta s}\frac{\Delta\boldsymbol{r}_n}{\|\Delta\boldsymbol{r}_n\|} \cdot \frac{\Delta\boldsymbol{r}_{n-1}}{\|\Delta\boldsymbol{r}_{n-1}\|} + \frac{\|\Delta\boldsymbol{r}_{n-1}\| - \Delta s}{\Delta s}\right]\frac{\Delta\boldsymbol{r}_{n-1}}{\|\Delta\boldsymbol{r}_{n-1}\|}, \tag{3.4}$$

whereas for $n = N$, one has

$$\boldsymbol{f}_N^{\parallel} = -K\frac{(\|\Delta\boldsymbol{r}_{N-1}\| - \Delta s)}{\Delta s}\frac{\Delta\boldsymbol{r}_{N-1}}{\|\Delta\boldsymbol{r}_{N-1}\|}. \tag{3.5}$$

Using (3.3) and (3.4)–(3.5), $\boldsymbol{f}_n$ can be evaluated sequentially from the filament tip (by decreasing order of n) in terms of the filament kinematic variables $\boldsymbol{r}_m$, $m \geqslant n-1$.

To solve (2.2)–(2.3), we use a one-dimensional distribution of regularized stokeslets along the centreline of the filament together with an 'image' distribution to impose the no-slip boundary conditions at the $z = 0$ plane (Cortez & Varela 2015). The regularized stokeslets are placed at the centre $\boldsymbol{r}_n$ of each segment. The strength of the regularized stokeslet at $\boldsymbol{r}_n$ is equal to the discrete force $\boldsymbol{f}_n$, and the fluid velocity generated by the filament at an arbitrary position $\boldsymbol{x}$ in the fluid domain is given by $\boldsymbol{u}(\boldsymbol{x}) = \sum_{n=1}^{N} \boldsymbol{G}(\boldsymbol{x} - \boldsymbol{r}_n) \cdot \boldsymbol{f}_n$, where $\boldsymbol{G}(\boldsymbol{x} - \boldsymbol{r}_n)$ is the Green's tensor for the regularized stokeslet near a wall (Ainley *et al.* 2008). We substitute this expression for the fluid velocity into (2.3), recalling (3.3) and (3.4)–(3.5) to express $\boldsymbol{f}_n$ in terms of the filament position $\boldsymbol{r}_m$. This yields a set of coupled equations for the filament dynamics that we evolve forwards in time using the forward Euler method. Initial conditions for this system are the configuration of the filament $\boldsymbol{r}(s, t)$ and the state variable $\alpha = \pm 1$.

In all numerical simulations, we fix the target angles at $\Theta = 0.15\pi$, we use $N = 20$ segments of length $a = 1/20$ to discretize the filament, and we set the regularization parameter of the stokeslet to be equal to a. The tensile stiffness $K = 5000$ is a numerical parameter chosen to keep the length of the filament almost constant. The filaments are initialized in straight configuration normal to the wall. Here, the time step is 0.2×10^{-4} and the system is integrated to $T = 20$, which is sufficient to capture the long-time dynamics; see table 2 for a summary of all parameter values.

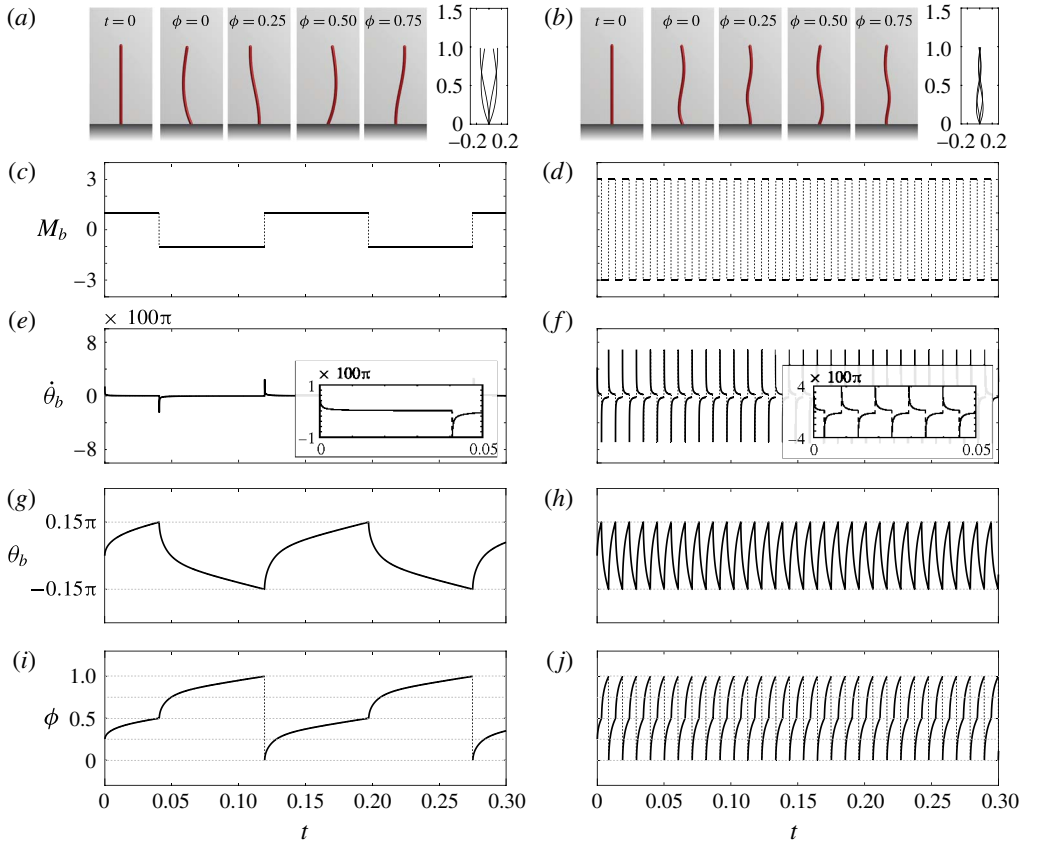

FIGURE 2. (Colour online) Filament dynamics for (a,c,e,g,i) $M_b = 1$ and (b,d,f,h,j) $M_b = 3$. From top to bottom: snapshots of the filament deformations, configuration-dependent moment M_b, angular velocity $\dot{\theta}_b$, angle θ_b and phase ϕ at the base of the filament as functions of time. Note that the frequency of oscillations is not known *a priori*, only the switching angles $\Theta = \pm 0.15\pi$.

4. Deformation of a single filament

We examine the motion of a single filament actively driven at its base by $\boldsymbol{M}_b = \alpha M_b \boldsymbol{e}_2$ $(\alpha = \pm 1)$ that switches direction at $\Theta = \pm 0.15\pi$. Figure 2 shows the deformations and time evolution of the filament for two distinct values of the bending moment: (a,c,e,g,i) $M_b = 1$ and (b,d,f,h,j) $M_b = 3$. In each case, the moment $\boldsymbol{M}_b$ is constant in magnitude between switches (figure 2*c*,*d*). In response, the angular velocity $\dot{\theta}_b$ slows down after each switching event (figure 2*e*,*f*). This decrease in $\dot{\theta}_b$ is induced by the internal restoring moment due to the filament elasticity, which acts in the opposite direction to $\boldsymbol{M}_b$.

We introduce the phase variable $\phi \in [0, 1]$ as a linear interpolation of θ_b between the two target angles $\pm\Theta$,

$$\phi = \frac{\Theta + \alpha\theta_b}{4\Theta} + \frac{1-\alpha}{4} = \begin{cases} \dfrac{\Theta + \theta_b}{4\Theta}, & \alpha = 1, \\ \dfrac{3\Theta - \theta_b}{4\Theta}, & \alpha = -1. \end{cases} \tag{4.1}$$

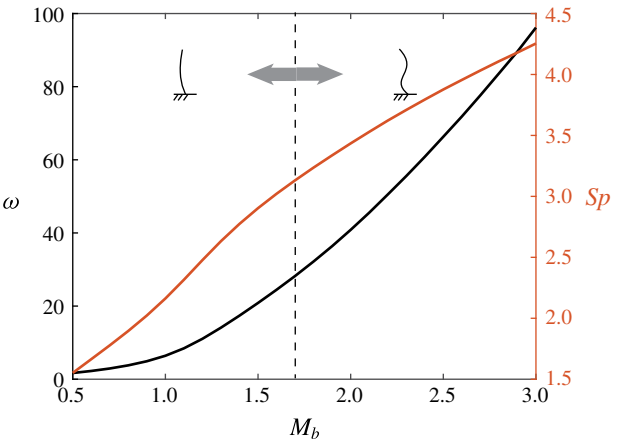

FIGURE 3. (Colour online) Beating frequency ω and Sperm number Sp of a single filament as a function of bending moment at the base M_b.

Parameter	Symbol	Dimensionless value
Number of segments per filament	N	20
Segment length	$\Delta s = a$	5×10^{-2}
Time step	Δt	2×10^{-5}
Total integration time	T	20
Target angle	Θ	0.15π
Magnitude of base moment	M_b	0.6–3.0
Filaments separation distance	d	0.4–1.1

TABLE 2. Dimensionless parameters used in the simulations (ℓ, μ and B are normalized to 1).

By definition, the values of ϕ lie in [0, 0.5] when the base moment is positive ($\alpha = 1$) and $\phi \in [0.5, 1]$ when the base moment switches to negative ($\alpha = -1$). Thus, the phase variable ϕ is monotonic in time over one oscillation period (see figure 2*i*,*j*) and, as a result, it can be viewed as a time reparametrization for examining the long-term periodic behaviour of the filament. We therefore label the snapshots in figure 2(*a*,*b*) by their phase ϕ.

The frequency of switching in the drive is a property of the system that depends on the system's parameters, including the magnitude of the base moment M_b. Figure 2 indicates that for $M_b = 1$, the base angle θ_b takes longer time to reach $\pm\Theta$ than for $M_b = 3$. To quantify the frequency ω of switching, we define it as the number of left-side switching events per unit time, averaged over late-time behaviour. Figure 3 depicts ω as a function of M_b. The frequency ω increases monotonically with M_b as well as the waviness of the filament. For M_b larger than 1.7, the curvature along the filament ($0 < s < \ell$) changes sign at least once, indicating a clear travelling-wave pattern. The switching frequency can be mapped to a Sperm number $Sp = (\ell^4 \xi_\perp \omega / B)^{1/4}$, defined as the ratio between the filament length and the elasto-viscous penetration length (Wiggins & Goldstein 1998; Lagomarsino, Capuani & Lowe 2003; Eloy & Lauga 2012). Here, $\xi_\perp = 4\pi\mu/\ln(2\ell/a)$ is the local drag coefficient perpendicular to the filament direction (Lauga & Powers 2009).

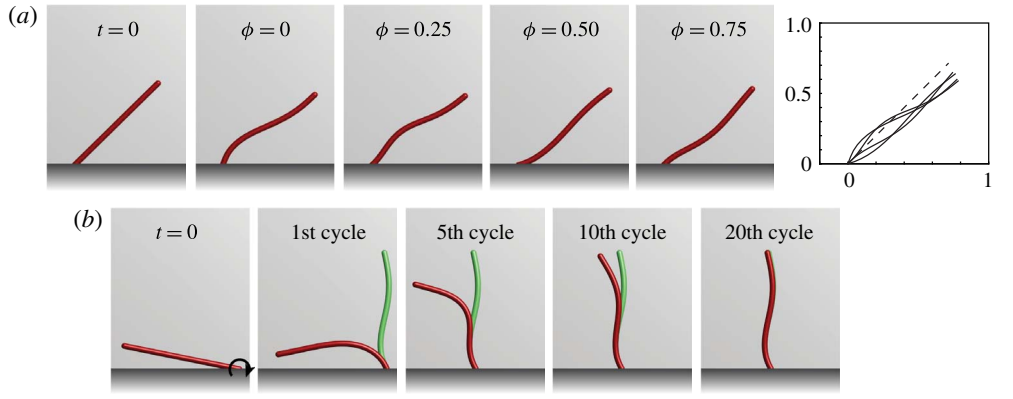

FIGURE 4. (Colour online) (*a*) Filament with tilted angles produce asymmetric beating patterns. Here $M_b = 3$, target angles are $\pi/4 \pm \Theta$. The dashed line shows the average orientation $\pi/4$. (*b*) The filament with $M_b = 3$ recovers the same beating pattern when starting from a perturbed initial condition; the long-term beating pattern is shown in green for comparison. Filaments with lower base moment converge to the long-term beating pattern within fewer cycles (see supplementary movies 1–4 available at https://doi.org/10.1017/jfm.2017.816).

The Sperm number Sp increases monotonically with M_b, ranging from 1.6 to 4.3 for $M_b \in [0.5, 3]$. This range of Sperm numbers is consistent with those observed empirically in flagella and cilia. For example, the wild-type *Chlamydomonas* has a beating frequency of 60–80 Hz (Leptos *et al.* 2013), which yields a Sperm number $Sp \approx 3$, given the characteristic parameters listed in table 1.

Although the Sperm number is comparable to that of cilia and flagella, the filament deformations deviate from those observed in nature in that the amplitude of the travelling wave decreases towards the tip. This is due to the fact that the model considers a driving moment at the base only, while, in many biological filaments, the moments are distributed along the whole filament. In the model, the beating pattern is related to the choice of the target angle Θ; larger Θ produces beating patterns with high curvature. Further, the filament deformations are symmetric because the switching orientations $\pm\Theta$ are equal and opposite. To break this symmetry, it suffices to tilt the angle about which the geometric switch is applied by setting $\Theta_{left} = 0.1\pi$ and $\Theta_{right} = 0.4\pi$ as shown in figure 4(*a*). Hereafter, we restrict our discussion to the symmetric case. Finally, we note that the long-term behaviour of the filament depends on M_b but it is independent of the filament initial configuration, as illustrated in figure 4(*b*).

5. Synchronization of two filaments

We consider the behaviour of two hydrodynamically coupled, elastic filaments separated by a distance d and subject to the same moment M_b at their base. We set the separation distance to be large enough ($d > 0.4$) so that the two filaments do not intersect.

Figure 5 shows the long-term behaviour of two filaments that start in a nearly anti-phase configuration; the left filament, referred to as filament 1, is initially straight and moving to the right ($\alpha_1(0) = 1$) whereas the right filament, or filament 2, is initially moving to the left ($\alpha_2(0) = -1$) such that the phase difference is equal to $\Delta\phi(0) =$

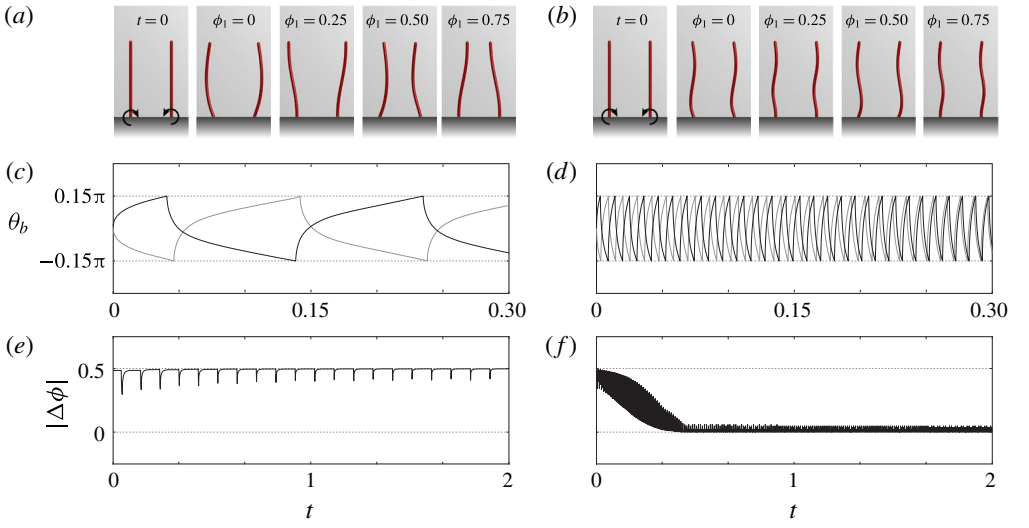

FIGURE 5. (Colour online) Long-term dynamics of a pair of filaments with (*a*,*c*,*e*) $M_b = 1$ and (*b*,*d*,*f*) $M_b = 3$ for $d = 0.7$ and $\Delta\phi(0) = 0.49$. (*a*,*b*) Beating patterns at four different phases ($\phi_1 = 0, 0.25, 0.5, 0.75$). (*c*,*d*) Base angles θ_b as a function of time for $0 < t < 0.3$ (to highlight transient behaviour). (*e*,*f*) Phase difference $|\Delta\phi|$ for $0 < t < 2$. See supplementary movies 5 and 6.

$\phi_2(0) - \phi_1(0) = 0.49$. Here, the state variables α_1 and α_2 and phase variables ϕ_1 and ϕ_2 for filaments 1 and 2 are defined as in (4.1). This initial configuration corresponds to a small perturbation away from the anti-phase configuration for which $\Delta\phi = 0.5$. The coupling between the two filaments is due to hydrodynamic interactions only.

The two filaments exhibit anti-phase synchronization for $M_b = 1$ and $d = 0.7$ as shown in figure 5(*a*,*c*,*e*), whereas for $M_b = 3$ the two filaments depart from their anti-phase initial conditions and approach in-phase synchronization as shown in figure 5(*b*,*d*,*f*). These modes of synchronization are quantified in figure 5(*e*,*f*). In both cases, the shapes of the filaments show no significant difference compared to those exhibited by the single filaments.

To quantify the long-term synchronization mode between the two filaments, we adapt the synchronization order parameter Q proposed in Kotar *et al.* (2010). Namely, we let

$$Q = \frac{-1}{T - T^*} \int_{T^*}^{T} \alpha_1(t)\alpha_2(t)\,\mathrm{d}t, \tag{5.1}$$

where T is the total integration time, and T^* is chosen to ensure that transient behaviour is excluded. By construction, one has $-1 \leqslant Q \leqslant 1$, where $Q = -1$ describes exactly in-phase motions while $Q = 1$ corresponds to exactly anti-phase motions. In the simulations, we set $T^* = 15$ and $T = 20$ time units, respectively; the filaments are said to be in-phase if $Q \in [-1, -0.5]$ and anti-phase if $Q \in [0.5, 1]$.

We fix the separation distance between the filaments at $d = 0.7$ and investigate the effect of the bending moment M_b on the long-term synchronization modes between the two filaments. We consider in-phase and anti-phase initial conditions $\Delta\phi(0) = 0$ and $\Delta\phi(0) = 0.5$, respectively, as well as small perturbations $\Delta\phi(0) = 0.01$ and $\Delta\phi(0) = 0.49$ away from these configurations. Figure 6(*a*) depicts the synchronization

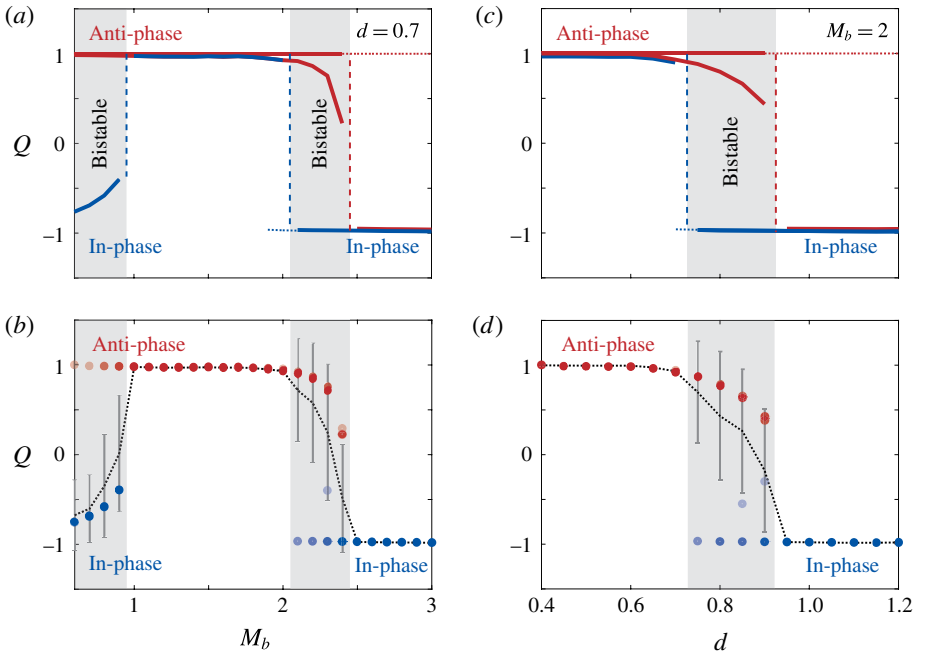

FIGURE 6. (Colour online) Synchronization order parameter Q as a function of (a,b) bending moment M_b and (c,d) separation distance d. (a,c) In-phase initial conditions are shown in blue and anti-phase in red. (b,d) Mean $\langle Q \rangle$ (dotted line) and standard deviation SD(Q) (grey error bars) corresponding to 20 random initial conditions; Q values are shown as blue and red dots, with colour intensity proportional to the percentage of initial conditions resulting in these values.

order parameter Q versus M_b shown in blue for $\Delta\phi(0) = 0$ and $\Delta\phi(0) = 0.01$ and in red for $\Delta\phi(0) = 0.5$ and $\Delta\phi(0) = 0.49$. When starting at $\Delta\phi = 0.5$, the filaments always synchronize anti-phase. However, this anti-phase synchronization becomes unstable for large M_b (dashed red line) because the filaments shift to in-phase synchronization under a small perturbation in the initial conditions ($\Delta\phi(0) = 0.49$). On the other hand, when starting at $\Delta\phi = 0$ and $\Delta\phi = 0.01$, the filaments synchronize in-phase for small M_b, shift to anti-phase synchronization as M_b increases, and shift back to in-phase synchronization as M_b increases further. For $0.6 \leqslant M_b \leqslant 0.9$ and $2.1 \leqslant M_b \leqslant 2.4$, the filaments exhibit both stable in-phase and stable anti-phase synchronization depending on initial conditions. To better understand the sensitivity of these synchronization modes to perturbations in the initial conditions, we perform Monte Carlo simulations with initial conditions randomly chosen from a uniform distribution function $\Delta\phi(0) \in \mathcal{U}(-0.5, 0.5)$. Statistical results of the synchronization modes based on 20 Monte Carlo simulations are shown in figure 6(b). Dotted lines and error bars depict the mean $\langle Q \rangle$ and standard deviation SD(Q) of the synchronization order parameter, respectively. Overlaid blue and red dots are the distributions of the Monte Carlo simulations, coloured in blue and red according to the emergent synchronization modes (blue for in-phase and vice versa). The colour intensity of the dots represents the fraction of simulations corresponding to a particular Q value – lighter colour means fewer simulations out of 20 total number of simulations. The bistable regions where both red and blue dots coexist are consistent

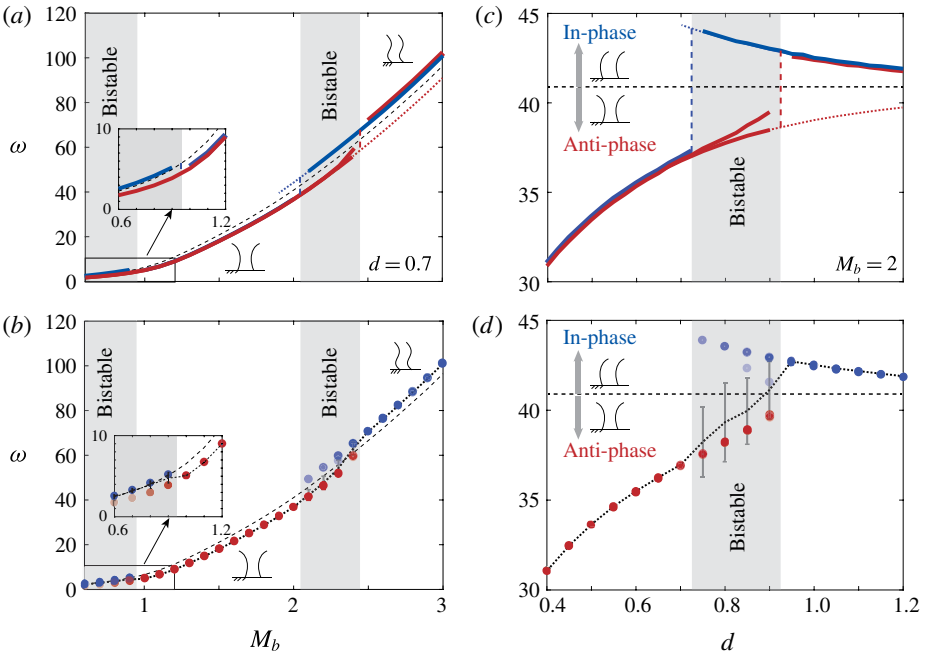

FIGURE 7. (Colour online) Beating frequency ω as a function of (a,b) bending moment M_b and (c,d) separation distance d. (a,c) In-phase initial conditions are shown in blue and anti-phase in red. (b,d) Mean $\langle\omega\rangle$ (dotted line) and standard deviation SD(ω) (grey error bars) corresponding to 20 random initial conditions; ω values are shown as blue and red dots, with colour intensity proportional to the percentage of initial conditions resulting in these values. In all panels, the frequency of a single filament (dashed black line) is superimposed for comparison.

with the results in figure 6(a). In the bistable regions, the synchronization mode is sensitive to initial conditions.

To explore the effect of the separation distance d between the filaments on the emergent synchronization modes, we fix the magnitude of the bending moment at $M_b = 2$ and plot the synchronization order parameter Q versus d in figure 6(c,d). For small d, all initial conditions lead to anti-phase synchronization. As d increases, both in-phase and anti-phase synchronizations coexist, depending on initial conditions, and as d increases further, only in-phase synchronization are observed. The Monte Carlo simulations shown in figure 6(d) are consistent with these findings. In the limit $d \to \infty$, the two filaments maintain their initial phase difference. In other words, as $d \to \infty$, the two filaments will take an infinitely long time to synchronize.

In figure 7, we report the values of the emergent beating frequencies for the cases considered in figure 6 and compare these values to the case of a single filament from figure 3, which we show in black dashed lines in figure 7. The beating frequencies for the pair of filaments are either faster or slower than the single filament depending on their synchronization modes: anti-phase filaments beat at lower frequencies because the two filaments 'work against each other', while in-phase filaments beat at higher frequencies because they 'work together'. In particular, in anti-phase beating, the two fibres are compressing and extending fluid elements in the region between them; while for in-phase beating, the fluid and the filaments move together. In the limit $d \to \infty$,

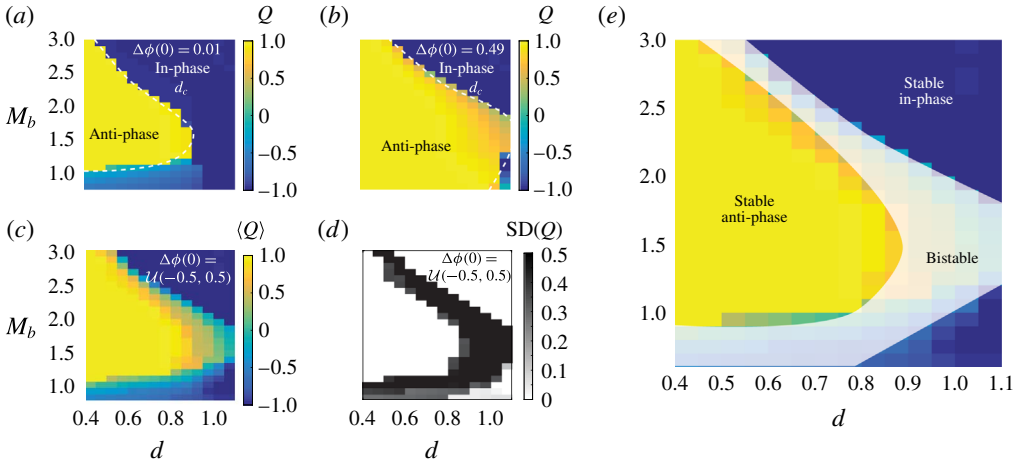

FIGURE 8. (Colour online) Synchronization order parameter of two filaments as a function of bending moment M_b and separation distance d for (a) nearly in-phase ($\Delta\phi(0) = 0.01$), (b) nearly anti-phase ($\Delta\phi(0) = 0.49$), and (c,d) 20 randomly chosen initial conditions. Here $\langle Q \rangle$ and SD(Q) are the mean and standard deviation of synchronization order parameter. High SD(Q) indicates sensitivity to initial conditions. (e) In-phase, anti-phase and bistable regions obtained by overlaying (c) and (d).

the beating frequency for the pair of filaments converges to the beating frequency of a single filament.

Figure 8 shows the synchronization order parameter Q over the parameter space (d, M_b); figure 8(a) shows Q for nearly in-phase initial conditions $\Delta\phi(0) = 0.01$ and figure 8(b) for nearly anti-phase initial conditions $\Delta\phi = 0.49$. Figures 8(c) and 8(d) show the mean and standard deviation, respectively, of Q for 20 Monte Carlo simulations with initial phase differences chosen from a uniform distribution $\mathcal{U}(-0.5, 0.5)$. Taken together, these results imply that the parameter space can be divided into three distinct regions: a stable anti-phase region where $\langle Q \rangle \in [0.5, 1]$ and SD(Q) < 0.2; a stable in-phase region where $\langle Q \rangle \in [-1, -0.5]$ and SD(Q) < 0.2; and a bistable region where $\langle Q \rangle \in [-0.5, 0.5]$ and SD(Q) > 0.2, in which the synchronization states are sensitive to the initial phase differences. The three regions are illustrated in figure 8(e).

6. Shape-dependent oscillators

In the geometric-switch model proposed by Kotar *et al.* (2010) and Bruot *et al.* (2012), a rigid spherical particle is free to move along one direction, say the x-axis, under the influence of a driving force F that switches direction when the particle position reaches predefined target positions. Here, we develop a phenomenological model, based on the geometric switch oscillator, that accounts for the filament's elasticity and shape changes in terms of a 'lumped' shape variable, which we denote by s (not to be confused with the filament's arclength s); see figure 1(c). We propose the coupled position–shape system of equations

$$\left.\begin{aligned} \xi(\mathrm{s})\dot{x} &= -k\mathrm{s} + \alpha F, \\ \tau\dot{\mathrm{s}} &= -\mathrm{s} + \alpha F. \end{aligned}\right\} \tag{6.1}$$

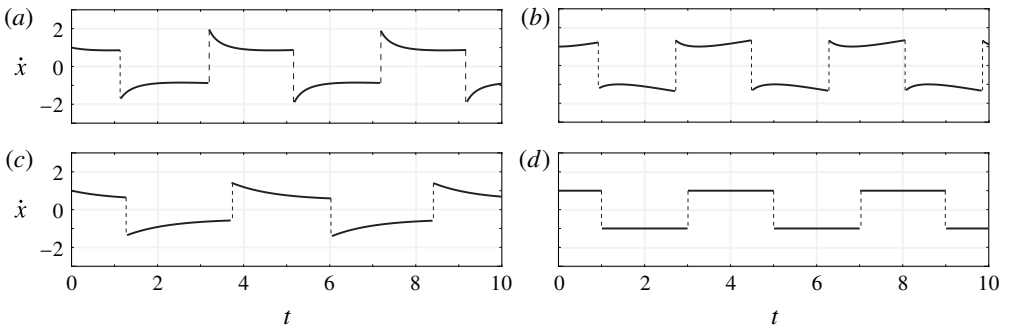

FIGURE 9. Velocity evolution $\dot{x}$ versus time t of the single shape-dependent oscillator for: (*a*) shape-dependent oscillator, $b = 0.5$, $k = 0.5$; (*b*) no restoring force, $b = 0.5$, $k = 0$; (*c*) constant drag coefficient, $b = 0$, $k = 0.5$; and (*d*) traditional oscillator, $b = 0$, $k = 0$. In all cases, $\tau = 1$, $\xi_o = 1$, $X_s = 1$ and $F = 1$.

The elastic 'particle' is subject to a configuration-dependent force αF, where the magnitude F is constant whereas α switches between $\{-1, 1\}$ as the particle position reaches a predefined oscillation amplitude $|x| = X_s$. For a rigid particle, the drive F is balanced by a hydrodynamic drag equal to $\xi\dot{x}$, where ξ is a constant (positive) drag coefficient. Elasticity introduces an internal restoring force that competes with the driving force and couples the shape s to the orientation dynamics. The elastic force is modelled via a spring with stiffness coefficient k that represents a 'lumped' elastic modulus of the filament. The drag coefficient ξ also depends on shape; it should be maximum when $\mathrm{s} = 0$, that is, when the filament is straight and moving transversely to itself, and minimum when the filament reaches its maximum deformation. It should also be symmetric under reflections from s to $-$s. We therefore set $\xi(\mathrm{s}) = \max(\xi_o - b\mathrm{s}^2, \epsilon)$, where the quadratic function $\xi_o - b\mathrm{s}^2$ is maximum at and symmetric about $\mathrm{s} = 0$ and the parameter b characterizes the dependence of ξ on shape. The lower bound $\epsilon > 0$ ensures that the drag coefficient ξ remains positive at all time.

The shape of the filament changes under the influence of the driving force but relaxes to its original shape when it is not actuated. In (6.1), we assume that αF drives the shape directly and that the shape s relaxes to the original shape s_o with constant relaxation parameter τ. For a fixed value of α, the solution to the shape equation is of the form $\mathrm{s} = \alpha F + (\mathrm{s}_o - \alpha F)e^{-t/\tau}$, where s relaxes to s_o when $F = 0$. For non-zero F, the force switches sign at $\pm X_s$, thus coupling position and shape. An alternative form of the shape equation in (6.1) could be written by using $\dot{x}$ to drive the shape dynamics instead of directly driving it by αF. Then, the shape equation becomes nonlinear. We chose the linear form in (6.1) because we are mainly interested in reducing the complexity of the dynamical system, while identifying the main physical mechanisms at play.

Figure 9(*a*) shows the typical evolution of $\dot{x}$ for the shape-dependent oscillator. The dynamics resembles qualitatively the dynamics of the full filament model shown in the second row of figure 2. Specifically, after each switch, the velocity $\dot{x}$ first experiences a sharp decrease and remains small until the next switch. This is a joint effect of the internal restoring moment $-k\mathrm{s}$ due to the filament elasticity and the shape-dependent drag coefficient $\xi(\mathrm{s})$. If the restoring moment is eliminated ($k = 0$), the velocity profile changes such that it first decreases then increases (figure 9*b*),

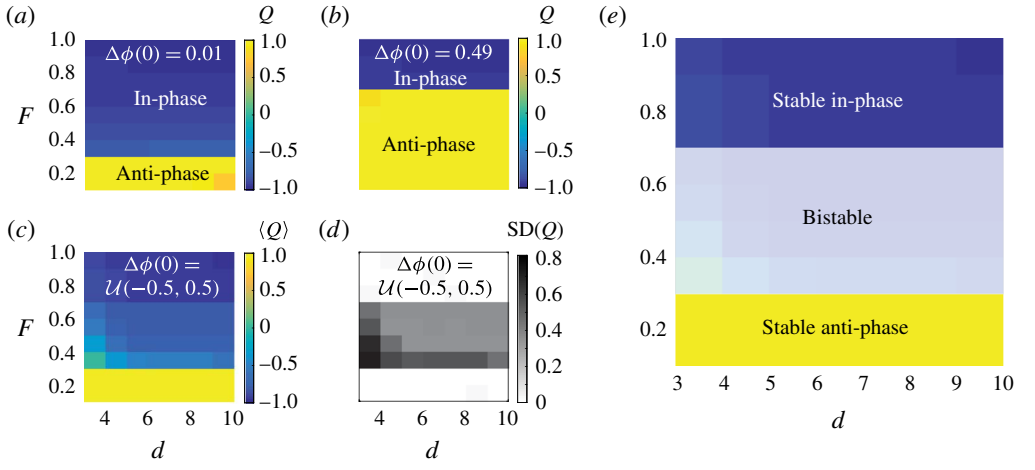

FIGURE 10. (Colour online) Synchronization modes of two shape-dependent oscillators as a function of applied force F and separation distance d for (a) nearly in-phase ($\Delta\phi(0) = 0.01$), (b) nearly anti-phase ($\Delta\phi(0) = 0.49$), and (c,d) 20 randomly chosen initial conditions. Here $\langle Q \rangle$ and SD(Q) are the mean and standard deviation of synchronization order parameter. High SD(Q) indicates sensitivity to initial conditions. (e) In-phase, anti-phase and bistable regions obtained by overlaying (c) and (d). In all simulations, $\tau = 1$, $b = 2$, $k = 0.1$, $X_s = 1$ and $\xi_o = 1$.

and if the drag coefficient is held constant ($b = 0$), the decrease in velocity after each switch is more gradual (figure 9c). In the case of the standard geometric switch $b = k = 0$, the velocity remains constant after each switch because the applied force considered here is constant (figure 9d).

We now consider two hydrodynamically coupled, shape-dependent oscillators,

$$\left.\begin{aligned} \xi(\mathrm{s}_i)[\dot{x}_i - v_j(x_i)] &= -k\mathrm{s}_i + \alpha_i F, \\ \tau\dot{\mathrm{s}}_i &= -\mathrm{s}_i + \alpha_i F. \end{aligned}\right\} \tag{6.2}$$

Subscripts $i, j = 1, 2$ are the oscillator indices and $v_j(x_i) = \dot{x}_j/|x_i - x_j|$ (with $i \neq j$) is the far-field approximation of the flow velocity generated by the motion of oscillator j at x_i. The state variable α_1 switches between $\{-1, 1\}$ once $|x_1| = X_s$, while α_2 switches between $\{-1, 1\}$ once $|x_2 - d| = X_s$, where d is the separation distance between the centres of the two oscillator trajectories.

If $b = k = 0$, the first equation in (6.2) is consistent with the geometric switch oscillators in Kotar *et al.* (2010) and Bruot *et al.* (2012) with one major distinction: here the applied force has constant magnitude. In their model, the applied force depends on the particle position, which determines the type of synchronization: the two oscillators synchronize anti-phase if the force magnitude decreases as the oscillator approaches X_s and in-phase if the force magnitude increases. For constant force, the two oscillators do not synchronize. Nowhere are bistable synchronizations observed. Consistent with their findings, when the shape changes are not accounted for ($b = k = 0$), the model in (6.2) exhibits no synchronization – the two oscillators maintain their initial phase difference for all time. However, when shape changes are considered ($b \neq 0$ and $k \neq 0$), multiple synchronization modes can arise depending on the parameter values and initial conditions, as shown in figure 10.

Figures 10(*a*) and 10(*b*) show the synchronization order parameter Q as a function of the force magnitude F and separation distance d for two sets of initial conditions $\Delta\phi(0) = 0.01$ and $\Delta\phi(0) = 0.49$, respectively. For both initial conditions, in-phase synchronization is favoured as F increases, albeit for different values of F. This tendency to synchronize in-phase at larger F is consistent with the trend observed in the full filament model. Figures 10(*c*) and 10(*d*) show the results of 20 Monte Carlo simulations with random initial conditions taken from a uniform distribution function: a stable anti-phase region is observed for $F < 0.3$, a stable in-phase region for $F > 0.7$, and a bistable region for $0.3 < F < 0.7$. The three regions are illustrated in figure 10(*e*).

The simple model in (6.2) captures some of the main features of the full filament model. In particular, it shows the presence of regions where in-phase and anti-phase oscillations are both stable, depending on initial conditions. This bistability is the product of the coupling between hydrodynamic interactions and shape changes. In fact, if the restoring force due to elasticity is eliminated ($k = 0$ but $b > 0$), the oscillators always synchronize in phase. Meanwhile, if the dependence of drag on shape is eliminated ($b = 0$ but $k > 0$), the oscillators always synchronize anti-phase. The two types of synchronization modes are observed only when the two effects of k and b are present. These findings imply that the two different synchronization modes observed in the simplified shape-dependent oscillators and in the full filament model are due to the interplay between elasticity, shape-dependent drag and hydrodynamic coupling.

7. Discussion

The main contributions of this work can be summarized as follows.

(i) We proposed a model for elastic microfilaments of finite length submerged in viscous fluid; the filaments are attached to a wall and driven at their base by a bending moment that is geometrically triggered to switch direction as the filament approaches predefined target angles.

(ii) We considered full hydrodynamic interactions among and within filaments. Isolated filaments were shown to undergo long-term periodic deformations that are insensitive to initial conditions and whose waviness and frequency increased with increasing the intensity of the driving moment.

(iii) Pairs of filaments exhibit stable in-phase and anti-phase synchrony that are robust to initial perturbations; more interestingly, both in-phase and anti-phase synchronizations stably coexist in regions of the parameter space (driving moment versus separation distance), with in-phase synchrony associated with higher oscillation frequencies. These multiple synchronization modes are inherently nonlinear and cannot be captured in a linear stability analysis.

(iv) To explain the main mechanisms underlying the observed behaviour, we proposed a low-order model of an elastic 'particle' that accounts for shape changes in terms of a 'lumped' shape variable that is coupled to the particle's position. The simpler model recapitulates the behaviour observed in single and pairs of filaments and highlights the role of each component – elasticity, shape-dependent drag and hydrodynamic coupling – in the emergent behaviour.

Our low-order model is consistent with the geometric switch oscillators of Kotar *et al.* (2010) and Bruot *et al.* (2012). In the latter, the driving force depends on the particle configuration, and its functional form determines the type of synchronization:

two oscillators synchronize anti-phase if the magnitude of the driving force decreases as each oscillator approaches its switching positions; they synchronize in-phase if the force magnitude increases. Shifting between different synchronization modes requires changing the model of the driving force. In contrast, in our models, the magnitude of the drive is independent of configuration. Stable in-phase or anti-phase as well as bistable synchronization modes all arise without the need to change the functional form of the drive. A transition from in-phase to anti-phase synchrony can be induced either by varying the drive level or by perturbing the initial conditions at the same drive level. On a more abstract level, the dynamics in our models can be thought of as associated with one potential landscape with multiple local minima that can be visited by changing either the parameter values or the initial conditions.

These findings – namely, the coexistence of in-phase and anti-phase synchrony and the fact that in-phase synchrony is associated with higher frequencies and filament waviness (travelling-wave deformations) – are consistent with experimental observations in a *Chlamydomonas* biflagellate (Leptos *et al.* 2013). It was shown that flagella switch stochastically between anti-phase and in-phase states, and that the latter has a distinct waveform and significantly higher frequency (the notation in-phase and anti-phase is reversed in Leptos *et al.* (2013)). In the context of our model, such switching could occur due to random perturbations or by varying the intensity of the internal drive. This is in contrast to alternating between different models of the drive characterized by different modes of synchrony (Leptos *et al.* 2013). The distinction between these two views – keeping the same form of the drive or alternating between different drive forms – is fundamentally linked to admissible hypotheses on the physiological and biophysical mechanisms underlying the transition between different synchronization modes. For example, in light of our results, it is plausible that transitions in biflagellar synchrony are triggered purely mechanically, say by random noise in the medium, without biochemical changes that alter the driving forces, or physiologically by modifying either the intensity of the drive or the compliance of the flagella, without inducing new behaviour in the internal machinery.

In the alga biflagellate *Chlamydomonas*, mechanical coupling at the flagella base could be playing a role in flagellar synchronization (Friedrich & Jülicher 2012; Geyer *et al.* 2013; Quaranta *et al.* 2015; Wan & Goldstein 2016). Importantly, in-phase and anti-phase synchrony is also observed between a pair of pipette-held flagella of *Volvox* somatic cells, where the coupling is purely hydrodynamic (Wan & Goldstein 2016, supplementary movies 2 and 3).

The model presented here serves to demonstrate that the interplay between elasticity, hydrodynamics and geometry-dependent actuation could give rise to multiple synchronization modes. While, in itself, the model is not intended to faithfully describe biological cilia and flagella, the outcomes of the model could serve to guide future research and formulate new hypotheses regarding the mechanisms that drive and alter synchrony in biological and physical systems. For example, it would be interesting to revisit the pipette-held flagella of *Volvox* somatic cells and conduct systematic experiments for identifying the physical parameters leading to in-phase and anti-phase synchrony. It would also be interesting to develop experimental protocols for gradually increasing the activity of the molecular motors in reactivated axonemes as in Geyer *et al.* (2016) to gauge the effect of the actuation level on synchrony. From the modelling standpoint, future extensions of this work will account for more accurate models of the internal driving moments (Goldstein *et al.* 2016; Sartori *et al.* 2016), 3D filament deformations with torsion and twist (Olson, Lim & Cortez 2013; Man, Koens & Lauga 2016) and multiple interacting filaments with application to

metachronal coordination of cilia (Gueron & Levit-Gurevich 1999; Mitran 2007; Yang *et al.* 2008; Guo *et al.* 2014; Guo & Kanso 2016). Meanwhile, we are working on including mechanical coupling at the base of the filaments to emulate basal coupling in the ciliated cell and investigate its role in filament synchronization, in the presence and absence of fluid coupling. The low-order model also presents a rich framework in which to explore synchronization of multi-particle oscillators as in Vilfan & Jülicher (2006) and Uchida & Golestanian (2011).

Acknowledgements

This work was partially supported by the Army Research Office through the ARO Grant W911NF-16-1-0074 (to E.K.) and the National Science Foundation through the NSF INSPIRE Grant 170731 (to E.K.) and the NSF Grants DMR-1420073 (NYU MRSEC: M.S.), DMS-1463962 (to M.S.) and DMS-1620331 (to M.S.). The work of L.F. is partially supported by NSF DMS-1043626. The authors would like to thank Amy Buchmann and Ricardo Cortez for helpful conversations.

Supplementary movies

Supplementary movies are available at https://doi.org/10.1017/jfm.2017.816.

REFERENCES

AINLEY, J., DURKIN, S., EMBID, R., BOINDALA, P. & CORTEZ, R. 2008 The method of images for regularized stokeslets. *J. Comput. Phys.* **227** (9), 4600–4616.

AUDOLY, B. & POMEAU, Y. 2010 *Elasticity and Geometry: From Hair Curls to the Non-linear Response of Shells*. Oxford University Press.

BRENNEN, C. & WINET, H. 1977 Fluid mechanics of propulsion by cilia and flagella. *Annu. Rev. Fluid Mech.* **9** (1), 339–398.

BROKAW, C. J. 1971 Bend propagation by a sliding filament model for flagella. *J. Expl Biol.* **55** (2), 289–304.

BROKAW, C. J. 2009 Thinking about flagellar oscillation. *Cytoskel.* **66** (8), 425–436.

BRUMLEY, D. R., POLIN, M., PEDLEY, T. J. & GOLDSTEIN, R. E. 2012 Hydrodynamic synchronization and metachronal waves on the surface of the colonial alga *Volvox carteri*. *Phys. Rev. Lett.* **109** (26), 268102.

BRUMLEY, D. R., WAN, K. Y., POLIN, M. & GOLDSTEIN, R. E. 2014 Flagellar synchronization through direct hydrodynamic interactions. *eLife* **3**, e02750.

BRUOT, N. & CICUTA, P. 2016 Realizing the physics of motile cilia synchronization with driven colloids. *Annu. Rev. Condens. Matter Phys.* **7** (1), 323–348.

BRUOT, N., KOTAR, J., DE LILLO, F., LAGOMARSINO, M. & COSENTINO, C. P. 2012 Driving potential and noise level determine the synchronization state of hydrodynamically coupled oscillators. *Phys. Rev. Lett.* **109** (16), 164103.

BUCHMANN, A., CORTEZ, R. & FAUCI, L. 2017 A sliding-control switch alters the stability of synchronized states in an elasto-hydrodynamic model of actuated cilia. (submitted).

CHRISPELL, J. C., FAUCI, L. J. & SHELLEY, M. 2013 An actuated elastic sheet interacting with passive and active structures in a viscoelastic fluid. *Phys. Fluids* **25** (1), 013103.

CORTEZ, R. & VARELA, D. 2015 A general system of images for regularized stokeslets and other elements near a plane wall. *J. Comput. Phys.* **285**, 41–54.

ELFRING, G. J. & LAUGA, E. 2011 Synchronization of flexible sheets. *J. Fluid Mech.* **674**, 163–173.

ELOY, C. & LAUGA, E. 2012 Kinematics of the most efficient cilium. *Phys. Rev. Lett.* **109** (3), 038101.

FAUBEL, R., WESTENDORF, C., BODENSCHATZ, E. & EICHELE, G. 2016 Cilia-based flow network in the brain ventricles. *Science* **353** (6295), 176–178.

FRIEDRICH, B. M. & JÜLICHER, F. 2012 Flagellar synchronization independent of hydrodynamic interactions. *Phys. Rev. Lett.* **109** (13), 138102.

FULFORD, G. R. & BLAKE, J. R. 1986 Muco-ciliary transport in the lung. *J. Theor. Biol.* **121** (4), 381–402.

GEYER, V. F., JÜLICHER, F., HOWARD, J. & FRIEDRICH, B. M. 2013 Cell-body rocking is a dominant mechanism for flagellar synchronization in a swimming alga. *Proc. Natl Acad. Sci. USA* **110** (45), 18058–18063.

GEYER, V. F., SARTORI, P., FRIEDRICH, B. M., JÜLICHER, F. & HOWARD, J. 2016 Independent control of the static and dynamic components of the *Chlamydomonas* flagellar beat. *Current Biol.* **26** (8), 1098–1103.

GOLDSTEIN, R. E., LAUGA, E., PESCI, A. I. & PROCTOR, M. R. 2016 Elastohydrodynamic synchronization of adjacent beating flagella. *Phys. Rev. Fluids* **1** (7), 073201.

GOLDSTEIN, R. E., POLIN, M. & TUVAL, I. 2009 Noise and synchronization in pairs of beating eukaryotic flagella. *Phys. Rev. Lett.* **103** (16), 168103.

GOLDSTEIN, R. E., POLIN, M. & TUVAL, I. 2011 Emergence of synchronized beating during the regrowth of eukaryotic flagella. *Phys. Rev. Lett.* **107** (14), 148103.

GOLESTANIAN, R., YEOMANS, J. M. & UCHIDA, N. 2011 Hydrodynamic synchronization at low Reynolds number. *Soft Matt.* **7** (7), 3074–3082.

GRAY, J. 1928 *Ciliary Movement*. Cambridge University Press.

GUERON, S. & LEVIT-GUREVICH, K. 1999 Energetic considerations of ciliary beating and the advantage of metachronal coordination. *Proc. Natl Acad. Sci. USA* **96** (22), 12240–12245.

GUIRAO, B. & JOANNY, J.-F. 2007 Spontaneous creation of macroscopic flow and metachronal waves in an array of cilia. *Biophys. J.* **92** (6), 1900–1917.

GUO, H. & KANSO, E. 2016 Evaluating efficiency and robustness in cilia design. *Phys. Rev.* E **93** (3), 033119.

GUO, H., NAWROTH, J. C., DING, Y. & KANSO, E. 2014 Cilia beating patterns are not hydrodynamically optimal. *Phys. Fluids* **26** (9), 091901.

KIM, Y. W. & NETZ, R. R. 2006 Pumping fluids with periodically beating grafted elastic filaments. *Phys. Rev. Lett.* **96** (15), 158101.

KOTAR, J., LEONI, M., BASSETTI, B., LAGOMARSINO, M. C. & CICUTA, P. 2010 Hydrodynamic synchronization of colloidal oscillators. *Proc. Natl Acad. Sci. USA* **107** (17), 7669–7673.

LAGOMARSINO, M. C., CAPUANI, F. & LOWE, C. P. 2003 A simulation study of the dynamics of a driven filament in an Aristotelian fluid. *J. Theor. Biol.* **224** (2), 215–224.

LAUGA, E. & POWERS, T. R. 2009 The hydrodynamics of swimming microorganisms. *Rep. Prog. Phys.* **72** (9), 096601.

LEPTOS, K. C., WAN, K. Y., POLIN, M., TUVAL, I., PESCI, A. I. & GOLDSTEIN, R. E. 2013 Antiphase synchronization in a flagellar-dominance mutant of *Chlamydomonas*. *Phys. Rev. Lett.* **111** (15), 158101.

LINDEMANN, C. B. 1994 A 'geometric clutch' hypothesis to explain oscillations of the axoneme of cilia and flagella. *J. Theor. Biol.* **168** (2), 175–189.

MAN, Y., KOENS, L. & LAUGA, E. 2016 Hydrodynamic interactions between nearby slender filaments. *Europhys. Lett.* **116** (2), 24002.

METTOT, C. & LAUGA, E. 2011 Energetics of synchronized states in three-dimensional beating flagella. *Phys. Rev.* E **84** (6), 061905.

MITRAN, S. M. 2007 Metachronal wave formation in a model of pulmonary cilia. *Comput. Struct.* **85** (11), 763–774.

NIEDERMAYER, T., ECKHARDT, B. & LENZ, P. 2008 Synchronization, phase locking, and metachronal wave formation in ciliary chains. *Chaos Interdiscipl. J. Nonlinear Sci.* **18**, 0370128.

OLSON, S. D. & FAUCI, L. J. 2015 Hydrodynamic interactions of sheets versus filaments: synchronization, attraction, and alignment. *Phys. Fluids* **27** (12), 121901.

OLSON, S. D., LIM, S. & CORTEZ, R. 2013 Modeling the dynamics of an elastic rod with intrinsic curvature and twist using a regularized stokes formulation. *J. Comput. Phys.* **238**, 169–187.

OSTERMAN, N. & VILFAN, A. 2011 Finding the ciliary beating pattern with optimal efficiency. *Proc. Natl Acad. Sci. USA* **108** (38), 15727–15732.

POLIN, M., TUVAL, I., DRESCHER, K., GOLLUB, J. P. & GOLDSTEIN, R. E. 2009 *Chlamydomonas* swims with two 'gears' in a eukaryotic version of run-and-tumble locomotion. *Science* **325** (5939), 487–490.

QUARANTA, G., AUBIN-TAM, M.-E. & TAM, D. 2015 Hydrodynamics versus intracellular coupling in the synchronization of eukaryotic flagella. *Phys. Rev. Lett.* **115** (23), 238101.

RIEDEL-KRUSE, I. H., HILFINGER, A., HOWARD, J. & JÜLICHER, F. 2007 How molecular motors shape the flagellar beat. *HFSP J.* **1** (3), 192–208.

RÜFFER, U. & NULTSCH, W. 1985 High-speed cinematographic analysis of the movement of *Chlamydomonas*. *Cytoskel.* **5** (3), 251–263.

RÜFFER, U. & NULTSCH, W. 1987 Comparison of the beating of cis- and trans-flagella of *Chlamydomonas* cells held on micropipettes. *Cytoskel.* **7** (1), 87–93.

SARTORI, P., GEYER, V. F., SCHOLICH, A., JÜLICHER, F. & HOWARD, J. 2016 Dynamic curvature regulation accounts for the symmetric and asymmetric beats of chlamydomonas flagella. *eLife* **5**, e13258.

TAYLOR, G. 1951 Analysis of the swimming of microscopic organisms. *Proc. R. Soc. Lond.* A **209** (1099), 447–461.

TERAN, J., FAUCI, L. J. & SHELLEY, M. 2010 Viscoelastic fluid response can increase the speed and efficiency of a free swimmer. *Phys. Rev. Lett.* **104** (3), 038101.

UCHIDA, N. & GOLESTANIAN, R. 2011 Generic conditions for hydrodynamic synchronization. *Phys. Rev. Lett.* **106** (5), 058104.

UCHIDA, N. & GOLESTANIAN, R. 2012 Hydrodynamic synchronization between objects with cyclic rigid trajectories. *Eur. Phys. J.* E *Soft Matt.* **35** (12), 9813–9813.

VILFAN, A. & JÜLICHER, F. 2006 Hydrodynamic flow patterns and synchronization of beating cilia. *Phys. Rev. Lett.* **96** (5), 058102.

WAN, K. Y. & GOLDSTEIN, R. E. 2016 Coordinated beating of algal flagella is mediated by basal coupling. *Proc. Natl Acad. Sci. USA* **113** (20), E2784–E2793.

WAN, K. Y., LEPTOS, K. C. & GOLDSTEIN, R. E. 2014 Lag, lock, sync, slip: the many 'phases' of coupled flagella. *J. R. Soc. Interface* **11** (94), 20131160.

WIGGINS, C. H. & GOLDSTEIN, R. E. 1998 Flexive and propulsive dynamics of elastica at low Reynolds number. *Phys. Rev. Lett.* **80**, 3879–3882.

WOOLLEY, D. M., CROCKETT, R. F., GROOM, W. D. & REVELL, S. G. 2009 A study of synchronisation between the flagella of bull spermatozoa, with related observations. *J. Expl Biol.* **212** (14), 2215–2223.

XU, G., WILSON, K. S., OKAMOTO, R. J., SHAO, J.-Y., DUTCHER, S. K. & BAYLY, P. V. 2016 Flexural rigidity and shear stiffness of flagella estimated from induced bends and counterbends. *Biophys. J.* **110** (12), 2759–2768.

YANG, X., DILLON, R. H. & FAUCI, L. J. 2008 An integrative computational model of multiciliary beating. *Bull. Math. Biol.* **70** (4), 1192–1215.